Native defects in the Co_2TiZ (Z = Si, Ge, Sn) full Heusler alloys: Formation and influence on the thermoelectric properties

Voicu Popescu,[1,*] Peter Kratzer,[1] Sebastian Wimmer,[2] and Hubert Ebert[2]

[1]*Faculty of Physics and Center for Nanointegration (CENIDE), University of Duisburg-Essen, Lotharstraße 1, 47057 Duisburg, Germany*

[2]*Department Chemie/Physikalische Chemie, Ludwig Maximilian University Munich, 81377 Munich, Germany*

(Received 1 April 2017; revised manuscript received 4 July 2017; published 28 August 2017)

We have performed first-principles investigations on the native defects in the half-metallic, ferromagnetic full Heusler alloys Co_2TiZ (Z one of the group IV elements Si, Ge, Sn), determining their formation energies and how they influence the transport properties. We find that the Co vacancies (Vc_{Co}) and the Ti_{Sn} as well as the Co_Z or Co_{Ti} antisites exhibit the smallest formation energies. The most abundant native defects were modeled as dilute alloys, treated with the coherent potential approximation in combination with the multiple-scattering theory Green function approach. The self-consistent potentials determined this way were used to calculate the residual resistivity via the Kubo-Greenwood formula and, based on its energy dependence, the Seebeck coefficient of the systems. The latter is shown to depend significantly on the type of defect, leading to variations that are related to subtle, spin-orbit coupling induced changes in the electronic structure above the half-metallic gap. Two of the systems, Vc_{Co} and Co_Z, are found to exhibit a negative Seebeck coefficient. This observation, together with their low formation energy, offers an explanation for the experimentally observed negative Seebeck coefficient of the Co_2TiZ compounds as being due to unintentionally created native defects.

DOI: 10.1103/PhysRevB.96.054443

I. INTRODUCTION

Intermetallic ternary compounds often possess special electronic and magnetic properties that make them interesting for technological applications. They manifest, however, a natural tendency towards off-stoichiometry, predictable from thermodynamic theory, which creates natural (intrinsic) doping via vacancies, antisites, or swaps [1]. Therefore, thorough studies of native defects in these materials are required prior to their incorporation in actual devices. This holds particularly true for ferromagnetic half metals in view of possible defect states being introduced in the half-metallic gap. The present work addresses this issue for Ti-derived half-metallic Heusler alloys. To motivate this research, we briefly review the use of half metals in spintronics.

One class of such materials, under intense scrutiny in the last decades, is the Co-based Heusler alloys [2–4] crystallizing in the cubic $L2_1$ structure. Many of them are predicted to be half metallic, a property describing the particular arrangement of the electronic states in which one spin channel is characterized by metallic conductance while the other one is semiconducting. While this makes them highly attractive for spintronics and spin-caloric transport, technological achievements are still rare, owing to the intrinsic complexity of these compounds. For example, first-principles electronic structure calculations [5,6] predicted 100% spin polarization near the Fermi energy in Co_2MnSi, but it took several more years of research and advanced sample preparation to provide experimental evidence in either bulk or thin-film phases [7,8]. The theoretically predicted stability of the Co_2MnSi/MgO interface [9] soon found experimental validation [10]. As a result, several successful implementations of Heusler-based magnetic tunnel junctions (MTJs), with potential use as magnetic random access memory (MRAM), have been reported [7,11–13]. Consisting of Co_2MnSi, Co_2FeSi, or Fe_2CoSi with either MgO or Al-O barriers, they are all characterized by extremely large, several hundred percent, magnetoresistance ratios. Other envisioned functionalities of half-metallic Heusler compounds include the electrically [14] and thermally driven [15,16] spin injection or the magnetocaloric memory device [17], neither of which having been accomplished experimentally yet.

Apart from Mn and Fe, early transition metals such as titanium offer further possibilities to tune the half-metallic properties and thus to open up novel applications. Thin films of Co_2TiSi were grown on MgO [18] as well as on GaAs substrates [19]. In a previous study, we have proposed a thermal spin injector based on a thin, lattice-matched barrier layer of either Co_2TiSi or Co_2TiGe between metallic leads [16]. Moreover, we could show that, similarly to the insulator case, the loss of half-metallicity is localized within a few atomic layers in the proximity of the interface. Thus, its role in the filtering of transmission channels notwithstanding, we find the understanding of the *bulk* transport properties of particular importance for the design of Heusler-based heterostructures.

This aspect appears more critical when considering the example of the half-metallic Co_2TiZ compounds (Z = Si, Ge, and Sn), which have been the subject of an extensive and exhaustive study [20]. Ground-state properties, including stable crystal structure, lattice constants, or spin magnetic moments, derived from first-principles calculations agree with the experimental findings [3,20–22]. On the other hand, theory has failed so far to satisfactorily explain the transport properties of these systems, in particular the Seebeck coefficient, whose spin dependence is at the core of many spin-caloric proposed applications. While from the calculated electronic structure at and around the Fermi energy one would expect a positive Seebeck coefficient in all three Co_2TiZ compounds [16,20], measurements indicate negative values throughout the whole temperature range, reaching $-50\ \mu V/K$ in the case of Co_2TiSn close to its Curie temperature [20,23].

*voicu.popescu@uni-due.de

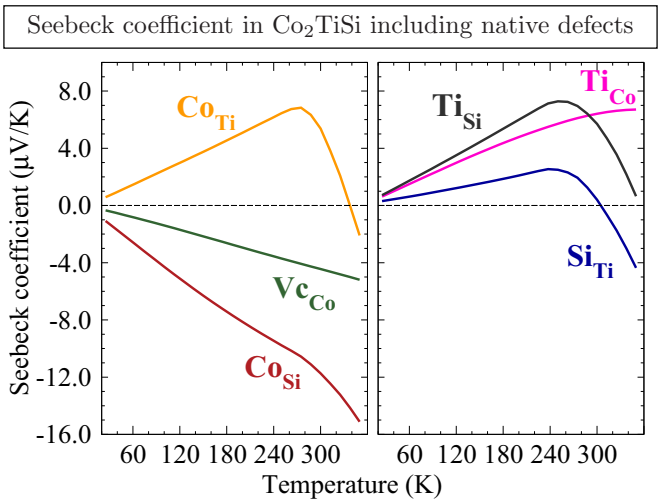

FIG. 1. Seebeck coefficient calculated for several off-stoichiometric native defects in Co_2TiSi, modeled as dilute alloys with 3% concentration. Note that the same scale is used for $S(T)$ in both panels.

This proved to be a rather puzzling finding in view of the useful and robust information that can be extracted from the Seebeck coefficient in semiconductors. There, a positive (negative) Seebeck coefficient can be unambiguously associated with a p-(n-)type doping of the semiconductor, a property that led to a rather common designation of conduction being either hole- or electron-like, depending on the sign of $S(T)$.

Unlike in semiconductors, where its size can be on the order of 10^2–10^3 μV/K, the Seebeck coefficient of metallic and half-metallic systems is much smaller and thus more sensitive even to small variations in the chemical composition of the sample. This appears indeed to be the case also for the Co_2TiZ Heusler alloys, for which small deviations from the 2:1:1 stoichiometry, deemed to qualify as "within the experimental error bars", have been reported [20].

To what extent the native defects occurring in the Co_2TiZ systems may influence the thermoelectric properties is illustrated by the calculated Seebeck coefficient displayed in Fig. 1. This figure, which summarizes the main results we report in this paper, shows the $S(T)$ curves corresponding to the Co_2TiSi Heusler compound including selected intrinsic defects at 3% atomic concentration. As can be seen, the calculations reveal the occurrence of a broad range of values, apparently varying between hole- and electron-like conduction, depending on the various off-stoichiometric deviations considered.

We investigate here native point defects in the full Heusler Co_2TiZ alloys, including vacancies (Vc) on different sublattices, antisites, and various sublattice swaps, with emphasis on their formation energy and their influence on both the electronic structure and transport properties of the host material. Owing to the close-packed character of the $L2_1$ structure we have deemed more complex defects, e.g., interstitial site occupation, dumbbells, or clustering effects, as being less likely to occur. Furthermore, we did not consider the formation and interaction of defect pairs. The main focus of our investigations is to establish a connection between the different features of the Seebeck coefficient seen in Fig. 1 with the defect-induced modifications in the electronic structure. In particular, we show that the negative $S(T)$ obtained for Co_Z and Vc_{Co} defects is due to *subtle changes of the electronic structure* that are mediated by spin-orbit coupling. Not only are these results in qualitative agreement with experiment; they also correspond to defects which show a small formation energy.

After briefly providing the computational details in Sec. II, the paper comprises two parts that, although methodologically independent, represent necessary logical steps in our quest. First, we employ pseudopotential-based, large-supercell total energy calculations to determine the formation energy [24–26] for all considered defects. The results, which are discussed in Sec. III, also imply the evaluation of the formation energy by taking into account the limits of the chemical potentials as obtained from separate calculations of competing binary and ternary compounds. For the second part, we select six different defects, found to exhibit formation energies under $\simeq 1$ eV, and model them as dilute alloys within the framework of the coherent potential approximation (CPA) [27–29] based on multiple-scattering theory as implemented in the full-potential spin-polarized relativistic Korringa-Kohn-Rostoker method [30–32]. A detailed analysis of the various influences these defects have on the electronic structure of the parent compound is provided in Sec. IV. This analysis, based on the Bloch spectral function, reveals signatures of several impurity bands appearing in the minority-spin channel, in the proximity of the half-metallic gap. With spin-orbit coupling causing majority-minority-band anticrossings right above the Fermi energy, we further show the effect of the different defects on these features, which may lead, in some cases, to an enhanced conductivity and a significant reduction of the spin polarization. The last section presents the results obtained for the electronic conductivity and the Seebeck coefficient in the dilute alloys from calculations performed employing the Kubo-Greenwood formula [33,34]. This approach has been already successfully applied to the study of various transport properties in Heusler alloys, ranging from longitudinal resistivity in $Co_2Mn(Al,Si)$ [35] to the anomalous Hall effect in $Co_2(Mn,Cr,Co)Al$ including native defects [36]. Applied here in the limit of dilute impurities, we include in the calculations the so-called vertex corrections [33] that are extremely important in this regime.

II. DETAILS OF THE CALCULATIONS

While our investigations consist of two separate steps, they do share the use of self-consistent field (SCF) calculations. These provide the crystal potential, determined within density functional theory (DFT), employing the generalized gradient approximation (GGA) parametrization for the exchange-correlation functional [37]. Specific details of the two adopted approaches are given in the following.

A. Formation energies from large supercells

The determination of the defect formation energies based on DFT is nowadays a standard approach, thoroughly described in the literature [24–26]. It involves calculations of the total energies, $E_{\rm tot}[H]$ and $E_{\rm tot}[H:D]$, in two systems: The clean host crystal H and the perturbed one $H:D$. These systems

are described by large supercells, constructed by repeatedly stacking the crystal unit cell along the spatial directions. The process of replacing host atoms by impurities D is regarded as a particle exchange, mediated by external reservoirs associated to each atomic species α. The requirement to describe the equilibrium between the perturbed host and the reservoirs calls for thermodynamic concepts. In the following, the thermodynamic equilibrium conditions are worked out at zero temperature and pressure. Denoting by E_α(bulk) the calculated total energy of the most stable condensed phase (solid or molecule) of element α, the chemical potential μ_α of each α reservoir can be expressed as

$$\mu_\alpha = E_\alpha(\text{bulk}) + \Delta\mu_\alpha, \tag{1}$$

with $\Delta\mu_\alpha$ the reduced chemical potential. In the present situation of the perturbed host in equilibrium with the reservoirs, it is required that

$$\Delta\mu_\alpha \leqslant 0 \quad \forall\alpha. \tag{2}$$

In other words, the E_α(bulk) provides an upper bound to the chemical potential, corresponding to the physical condition of atom α not precipitating into its stable phase.

With the notations introduced above, the formation energy $E_{\text{form}}[D]$ of a neutral defect D is obtained from

$$E_{\text{form}}[D] = E_{\text{tot}}[H:D] - E_{\text{tot}}[H] - \sum_\alpha N_\alpha E_\alpha(\text{bulk}) - \sum_\alpha N_\alpha \Delta\mu_\alpha, \tag{3}$$

where N_α is the number of atoms, either host or impurity, that were added to ($N_\alpha > 0$) or removed from ($N_\alpha < 0$) the supercell upon creating the perturbed system [24]. Since the N_α's depend on the chosen configuration and the total energies are calculated directly, it follows that, among the terms on the right-hand side of Eq. (3), the reduced chemical potentials $\Delta\mu_\alpha$ are the only independent variables, leading to the compact form

$$E_{\text{form}}[D] = \Delta E(H,D) - \sum_\alpha N_\alpha \Delta\mu_\alpha, \tag{4}$$

with

$$\Delta E(H,D) = E_{\text{tot}}[H:D] - E_{\text{tot}}[H] - \sum_\alpha N_\alpha E_\alpha(\text{bulk}). \tag{5}$$

The values of the reduced chemical potentials are subject to various constraints, one of which is given in Eq. (2) as an upper bound to $\Delta\mu_\alpha$. Additional bounds arise from the following requirements: First, thermodynamic equilibrium of the constituents with the host crystal must hold. Specific to the full Heusler alloys Co_2TiZ investigated here, this condition reads

$$2\Delta\mu_{\text{Co}} + \Delta\mu_{\text{Ti}} + \Delta\mu_Z = \Delta H(Co_2TiZ), \tag{6}$$

where $\Delta H(Co_2TiZ)$ is the formation enthalpy of the Co_2TiZ compound at zero temperature and pressure. Second, the reduced chemical potentials of either host or impurity atoms have to be in ranges where competing binary or ternary systems may not form. For a generic compound with chemical formula $Co_aTi_bZ_c$ and formation enthalpy $\Delta H(Co_aTi_bZ_c)$ one obtains

$$a\Delta\mu_{\text{Co}} + b\Delta\mu_{\text{Ti}} + c\Delta\mu_Z \leqslant \Delta H(Co_aTi_bZ_c). \tag{7}$$

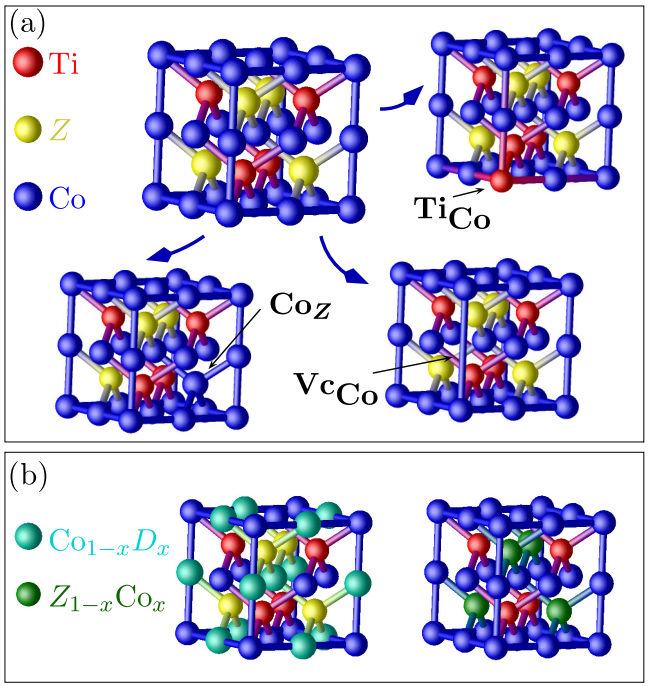

FIG. 2. (a) Structural model of the Co_2TiZ (Z = Si, Ge, Sn) full Heusler $L2_1$ structure and illustrative examples of some of the intrinsic defects investigated in this work. (b) Examples of unit cells used in the alloy modeling of the intrinsic defects in Co_2TiZ, accounting only for partial disorder: $Co(Co_{1-x}D_x)TiZ$ for a D atom in the Co sublattice (D_{Co}) and $Co_2TiZ_{1-x}Co_x$ for a Co atom in excess on the group IV element sublattice (Co_Z).

Combining all the constraints derived from the relations (2), (6), and (7) allows one to determine a stability range $\{\Delta\mu_{\text{Co}}, \Delta\mu_{\text{Ti}}, \Delta\mu_Z\}$ for which the investigated compound (here the Co_2TiZ Heusler alloy) may form under equilibrium growth conditions. For ternary compounds it is common, using Eq. (6), to eliminate one of the variables (in the following $\Delta\mu_Z$), leaving for both the stability range and the defect formation energy $E_{\text{form}}[X]$ only a two-dimensional explicit dependence (in the following $\{\Delta\mu_{\text{Co}}, \Delta\mu_{\text{Ti}}\}$).

B. Total energy calculations

The Co_2TiZ (Z = Si, Ge, Sn) compounds investigated here belong to the class of full Heusler alloys [4] of prototype Cu_2MnAl, crystallizing in the cubic $L2_1$ structure. This crystal structure, shown in Fig. 2(a), has a face-centered-cubic (fcc) primitive cell with four inequivalent atomic sites. It can be viewed either as four interpenetrating fcc sublattices, respectively occupied by the Co, Ti, Co, and Z atoms shifted against each other by (1/4,1/4,1/4) lattice constants, or as two interpenetrating CoTi and CoZ zinc-blende structures shifted by (0,0,1/2).

We have considered several off-stoichiometric native defects: (a) an additional Co, Ti, or Z atom occupying a different sublattice (in the following denoted as Co_{Ti}, Ti_{Co}, Z_{Co}, and so on), and (b) vacancies on one of the Co, Ti, and Z sites (labeled respectively as Vc_{Co}, Vc_{Ti}, Vc_Z). Stoichiometry-preserving configurations, in which two neighboring atoms from different sublattices are switching places (Co $\leftrightarrow$ Ti, $Z \leftrightarrow$ Ti, and Co $\leftrightarrow$

Z), were also investigated. Illustrative examples of the various systems are depicted in Fig. 2(a). Note that a 128-atom supercell (that is, larger than shown in the figure) was used in all calculations of the defect formation energy. On the other hand, the determination of the competing compounds formation enthalpy needed in Eq. (7) relied on their respective primitive cells.

In all cases, the total energies were calculated for spin-polarized systems in the scalar relativistic approximation (SRA) employing the plane-wave pseudopotential method as implemented in the Quantum Espresso code [38]. Wave functions and density have been expanded into plane waves up to cutoff energies of 40 Ry and 400 Ry, respectively. The neighborhood of atomic centers has been approximated by self-created ultrasoft pseudopotentials (USPPs) [39], as described previously in our study of the Al/Co_2TiZ heterostructures [16]. A Methfessel-Paxton smearing [40] of 10 mRy has been applied to the Brillouin zone (BZ) sampling performed with different Monkhorst-Pack k-point grids [41]. These were chosen in such a way that they did not include the Γ point and delivered well-converged total energies and potentials. In all systems, the lattice constants and the internal atomic positions have been accurately optimized using Hellmann-Feynman forces to reduce the force components below 1 mRy/a_0 and the energy changes below 0.1 mRy.

C. Alloy modeling for the calculation of transport properties

In a second step, we have determined the transport properties of the Co_2TiZ Heusler compounds in the presence of the intrinsic defects, which were modeled as off-stoichiometric dilute alloys within the CPA [27–29]. As shown schematically in Fig. 2(b), each defect was assigned a mixed occupation of a single sublattice in the $L2_1$ structure. We illustrate here examples of $Co(Co_{1-x}D_x)TiZ$ and $Co_2Ti(Z_{1-x}Co_x)$ chemical formulas, respectively describing the $Co_2TiZ{:}D_{Co}$ (D = Vc, Ti, Z) and $Co_2TiZ{:}Co_Z$ systems. The effect of a varying defect concentration was accounted for by considering different x values ($x = 0.01$, 0.03, and 0.05).

The calculations were based on a full-potential, spin-polarized relativistic implementation of the Korringa-Kohn-Rostoker Green function method (FP-SPR-KKR) [30–32]. We obtained the SCF charge density and potentials by integrating the Green function in the complex energy plane over a contour consisting of 36 points and applying an angular momentum cutoff of $l_{max} = 3$ for the Green function expansion. We need to emphasize here the importance of going beyond the atomic sphere approximation (ASA) when methods employing atom-centered basis functions are applied to Heusler alloys. Even in the case of the closed-packed $L2_1$ structure, ASA-based electronic structure calculations may fail to reproduce the full-potential (FP) results [42,43]. As pointed out by Picozzi *et al.* [42] such discrepancies originate from the appreciable asphericities that may be present in the charge density [44].

For all three parent compounds Co_2TiZ we calculated the equilibrium lattice constants by minimizing the total energy. The differences between the FP-SPR-KKR determined lattice constants and those obtained by the scalar-relativistic plane-wave approach were found to be in the range of $\simeq 0.025$ Å, with an overall agreement within 1% of the experimental results [20,45,46]. Including spin-orbit coupling (SOC) has therefore a very small influence on the computed equilibrium lattice parameters. We will show, however, that its role in the thermoelectric properties cannot be neglected.

The transport properties of the $Co_2TiZ{:}D$ systems were determined subsequently to the SCF calculations. More specific, the temperature-dependent longitudinal Seebeck coefficient $S_{ii}(T)$ (with $i = x$, y, or z the Cartesian coordinate) can be obtained from the diagonal elements of the energy-dependent conductivity tensor $\sigma_{ii}(E)$ [47]. Introducing the transport coefficients

$$L_{ij}^{(m)} = -\frac{1}{e}\int\left[\frac{\partial}{\partial E} f_0(E,\mu,T)\right](E-\mu)^m \sigma_{ij}(E)\,dE, \quad (8)$$

where $f_0(E,\mu,T)$ is the Fermi-Dirac distribution function with chemical potential μ at energy E for the temperature T, the Seebeck coefficient is given by

$$S_{ii}(T) = -\frac{1}{eT}\frac{L_{ii}^{(1)}}{L_{ii}^{(0)}} \quad (9)$$

with e the elementary charge [48]. In our calculations, the central quantity is represented by the electronic conductivity, obtained on the basis of the Kubo-Greenwood formula [33,34], appropriately extended for nonspherical potentials, and including the important contributions stemming from the so called vertex corrections [33]. At each energy argument, the diagonal elements of $\underline{\sigma}(E)$ are obtained through a BZ integral evaluated over a number of 2×10^6 k-points. For the energy integrals appearing in Eq. (8) we started by explicitly calculating $\underline{\sigma}(E)$ on an equidistant mesh of 1 mRy separation, then refining it to a 0.01 mRy resolution by linear interpolation. The integration boundaries around the chemical potential were set by the cutoff criterion $\partial f_0(E,\mu,T)/\partial E \geqslant 10^{-3}$ for a fixed electronic temperature T.

III. DEFECT FORMATION ENERGY RESULTS

We present in this section the results obtained by applying the *ab initio* thermodynamics concepts introduced above. After establishing the stability ranges by analyzing the competing binary and ternary compounds, we derive upper and lower boundaries for the defect formation energies E_{form}. We show that the smallest values of E_{form} occur for vacancies on Co sublattice (Vc_{Co}) followed by other defects, such as the Co antisites Co_{Ti} and Co_Z.

A. Boundaries of the reduced chemical potentials

The calculated stability domains for each of the Co_2TiZ full Heusler alloys are displayed in Fig. 3 as two-dimensional representations in the $(\Delta\mu_{Co}, \Delta\mu_{Ti})$ plane. Their construction is based on the numerical evaluation of Eqs. (6) and (7) with the corresponding (zero temperature and pressure) formation enthalpies provided in Table I. For consistency reasons, these were obtained using the same set of self-constructed pseudopotentials as employed in the supercell-related defect calculations, and were found in very good agreement with equivalent data available in various online repositories [49]. The list of possible competing binary phases in Table I is obviously not exhaustive. On one hand, we have only

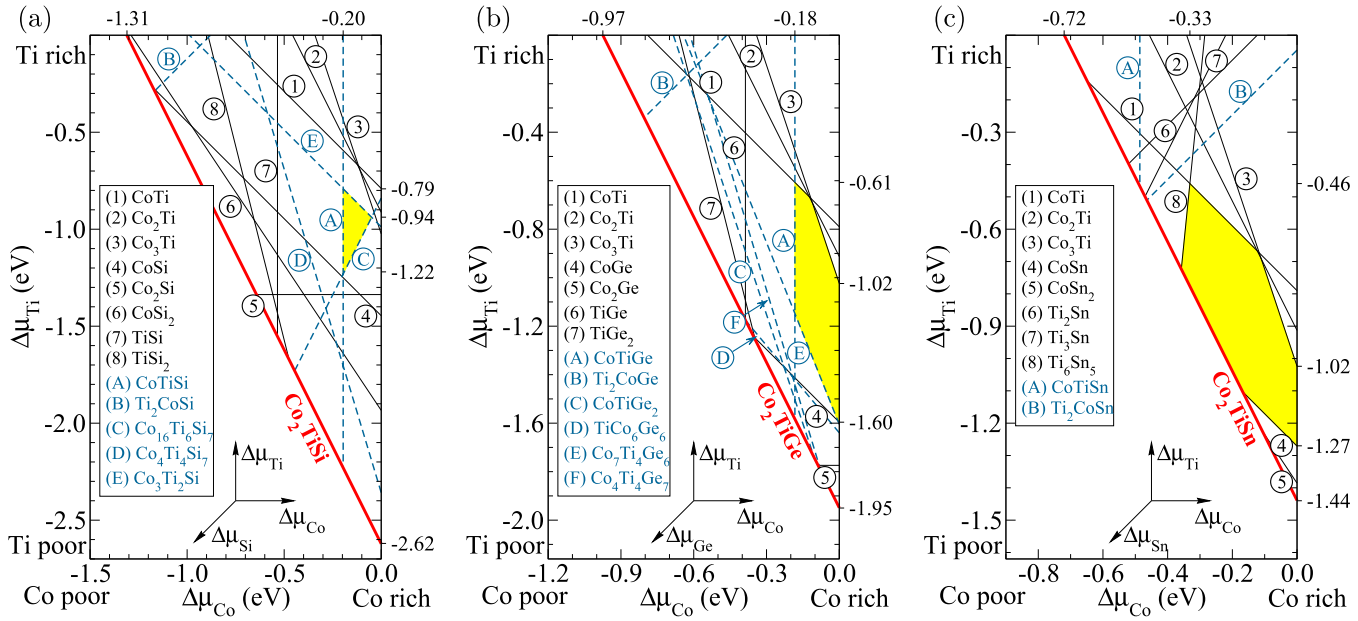

FIG. 3. The calculated stability regime for the full Heusler alloys Co_2TiZ (Z = Si, Ge, Sn) in the $(\Delta\mu_{Co}, \Delta\mu_{Ti})$ plane. From left to right: (a) Co_2TiSi, (b) Co_2TiGe, and (c) Co_2TiSn. The red (dark gray) thick line represents the equilibrium condition $2\Delta\mu_{Co} + \Delta\mu_{Ti} + \Delta\mu_Z = \Delta H(Co_2TiZ)$, while the shaded areas mark the $\Delta\mu_\alpha$ values (α = Co, Ti, Z) for which the Co_2TiZ compound may form under equilibrium growth conditions. This is determined by taking into account the additional boundaries set to the $\Delta\mu_\alpha$'s by the formation of the competing binary or ternary compounds accordingly listed in each panel. The equilibrium conditions for these phases, corresponding to an equality in Eq. (7), are represented by thin lines appropriately labeled using numbers (for the binaries) and letters (for the ternaries). The relative positioning of an assigned label with respect to the line it labels indicates the respective precipitation range of each system.

considered compounds known to exist. On the other hand, rather than exploring all possibilities, we only focused on those systems that pose restrictions for the reduced chemical potentials. In other words, from literature data we could conclude that certain stoichiometries will not give stricter boundaries than the ones already identified. This procedure appeared to be justified by the overall good agreement of our data with the previously published results.

The discussion of the results shown in Fig. 3 starts with some common features of the three panels. The stability triangles represent $(\Delta\mu_{Co}, \Delta\mu_{Ti}, \Delta\mu_Z)$ triplets for which the Co_2TiZ compound may form. They are defined by the upper bounds of $\Delta\mu_\alpha$ given in Eq. (2). As already mentioned, the $\Delta\mu_Z$ variable can be eliminated using the equilibrium condition (6), such that the $\Delta\mu_Z \leqslant 0$ constraint reduces to $2\Delta\mu_{Co} + \Delta\mu_{Ti} \geqslant \Delta H(Co_2TiZ)$. The equality sign is the equivalent of the thick red line in each panel of Fig. 3. Accounting for the formation of competing binary and ternary systems, according to Eq. (7), further reduces the allowed $\Delta\mu_\alpha$ values, leading to the arbitrarily shaped polygons highlighted by the shaded areas. Their boundaries, displayed as dashed and solid lines and appropriately labeled by the respective chemical formula in the figure, are briefly discussed below.

As can be seen in Fig. 3, for the Co_2TiGe and Co_2TiSn compounds $\Delta\mu_{Co} = 0$ remains as the upper bound, whereas $\Delta\mu_{Ti}$ is limited above by either CoTi, Co_2Ti, or Co_3Ti. Allowed $\Delta\mu_{Ti}$ values must fulfill the conditions

$$\Delta\mu_{Ti} \leqslant \Delta H(Co_aTi) - a\Delta\mu_{Co}\ (a = 1,2,3) \qquad (10)$$

over the various $\Delta\mu_{Co}$ intervals. Comparing our results with those of Chepulskii and Curtarolo [50] who calculated the full series of Co-Ti alloys, we find a very good agreement for all Co_aTi ($a = 1 \ldots 3$) systems [51]. For $CoTi_2$, on the other hand, these authors report a formation enthalpy of -0.873 eV/formula unit. It is easy to check, via Eq. (7), that the stable $CoTi_2$ bulk phase lies inside the area already covered by one of the Co_aTi compounds.

The Co_2TiSi exhibits the peculiar situation of the stability range being completely determined by the formation of ternary compounds: Co_3Ti_2Si and $Co_{16}Ti_6Si_7$ set the upper and lower boundaries of $\Delta\mu_{Ti}$, while the crossing of their equilibrium lines fixes the maximum $\Delta\mu_{Co}$ value at -0.05 eV. On the Co-poor (small $\Delta\mu_{Co}$) side, the lower boundary is set by the CoTiSi compound crystallizing in the orthorhombic $C23$ structure. Analogously, the ternary CoTiGe compound in the hexagonal $C22$ structure sets the lower boundary of $\Delta\mu_{Co}$ in the Co_2TiGe system. In contrast, CoTiSn, with its ground state the $C1_b$ (half-Heusler) structure, forms outside the Co_2TiSn stability range, with the Co-poor boundary determined by the Ti-Sn binaries. As seen in Table I, TiSi and TiGe both crystallize in the $B27$ structure. A stable phase of TiSn, on the other hand, is not known to exist, although investigations performed by Colinet *et al.* [52] on a series of Ti-Sn binaries predict a negative formation enthalpy for TiSn in various structures. While our calculations, performed for Ti_2Sn, Ti_3Sn, and Ti_6Sn_5 delivered formation enthalpies in close agreement with their results, we chose to set the stability boundary to that provided by the Ti_6Sn_5 compound.

In the Co-rich, Ti-poor range (bottom right corner), the formation of the Co_2TiGe and Co_2TiSn competes with that of the corresponding Co-Z binary compounds. In both cases the lower boundary of $\Delta\mu_{Ti}$ is set by CoGe or CoSn, leading to

TABLE I. The calculated formation enthalpy ΔH (in eV/formula unit) for the Co_2TiZ (Z = Si, Ge, Sn) full Heusler alloys as well as of various Co-Ti, Co-Z, Ti-Z, and Co-Ti-Z binary and ternary compounds which compete with the Co_2TiZ formation. For the latter we also include the equilibrium lattice constants used in this work as obtained either through the plane-wave pseudopotential method in the SRA (results labeled as QE) or the full potential SPR-KKR Green function approach (KKR). The calculated values are compared with the experimental data [45,46].

Compound (structure)	ΔH (eV/f.u.)	Lattice constant (Å)		
		QE	KKR	Experiment
Co_2TiSi ($L2_1$)	−2.62	5.756	5.780	5.74(0)
Co_2TiGe ($L2_1$)	−1.95	5.848	5.874	5.83(1)
Co_2TiSn ($L2_1$)	−1.44	6.092	6.119	6.07(3)
Compound (structure)	ΔH (eV/f.u.)		Compound (structure)	ΔH (eV/f.u.)
CoTi ($B2$)	−0.79		TiGe ($B27$)	−1.18
Co_2Ti ($C15$)	−0.91		$TiGe_2$ ($C54$)	−1.26
Co_3Ti ($L1_2$)	−1.02		Ti_2Sn ($B8_2$)	−1.00
CoSi ($B20$)	−1.18		Ti_3Sn ($D0_{19}$)	−1.19
Co_2Si ($C23$)	−1.29		Ti_6Sn_5 (hP22)	−4.34
$CoSi_2$ ($C1$)	−1.38		$Co_4Ti_4Si_7$ (tI60)	−11.28
CoGe ($B20$)	−0.35		$Co_{16}Ti_6Si_7$ (cF116)	−17.52
Co_2Ge ($B8_2$)	−0.18		Co_3Ti_2Si (hP12)	−3.61
CoSn ($B35$)	−0.17		$CoTiGe_2$ (oP48)	−1.85
$CoSn_2$ ($C16$)	−0.11		$Co_4Ti_4Ge_7$ (tI60)	−7.49
TiSi ($B27$)	−1.55		$TiCo_6Ge_6$ (hP13)	−3.50
$TiSi_2$ ($C54$)	−1.67		$Co_7Ti_4Ge_6$ (cI34)	−8.48
Ti_2CoSi ($L2_1$)	−1.74		CoTiSi ($C23$/oP12)	−2.43
Ti_2CoGe ($L2_1$)	−1.49		CoTiGe ($C22$/hP9)	−1.77
Ti_2CoSn ($L2_1$)	−0.67		CoTiSn ($C1_b$)	−0.95

the constraint

$$\Delta\mu_{Ti} \geqslant \Delta H(Co_2TiZ) - \Delta H(CoZ) - \Delta\mu_{Co}. \quad (11)$$

Having completely defined the boundaries for $\Delta\mu_{Co}$ and $\Delta\mu_{Ti}$ we note that these can also be transferred back to $\Delta\mu_Z$ via Eq. (6). In combination with the observed increase of $\Delta H(Co_2TiZ)$ within the Z = Si, Ge, Sn series, it becomes obvious, from Fig. 3, that Z-rich conditions can only be attained in the Co_2TiSn system. For Z = Si and Ge, either CoTiSi, CoSi, or $Co_7Ti_4Ge_7$ set an upper bound for $\Delta\mu_Z$.

We close the discussion on chemical potential boundaries by analyzing the formation enthalpy of the Ti_2CoZ systems, as competing inverse full Heusler alloys. These compounds are stable through the whole series of group IV elements Z, with the formation being subject to the condition $\Delta\mu_{Ti} \geqslant \Delta\mu_{Co} + [\Delta H(Ti_2CoZ) - \Delta H(Co_2TiZ)]$. According to our results shown in Table I, this condition [labeled (B) in Fig. 3] falls inside the Co_2TiZ stability triangle for all Z atoms. In all cases, however, it remains outside the shaded areas indicating that, while competing precipitation of Ti_2CoZ may occur, it requires significantly different growth conditions than the respective stable full Heusler alloy.

B. Formation energies of intrinsic defects in Co_2TiZ

We give in the following a survey of the calculated formation energies of all the defects considered. The results listed in Table II give the lower and upper bounds of the formation energy $E_{form}[D]$ and the reference energies $\Delta E(Co_2TiZ, D)$. The latter, defined by Eq. (5), implicitly contains system-specific information related to intrinsic mechanisms concerning the defect formation, such as equilibrium bond length and electronegativity. The former, obtained from Eq. (4) by inserting the extremum values of the $\sum_\alpha N_\alpha \Delta\mu_\alpha$ term, can be seen as the energy required to exchange particles with the reservoirs [26]. Our results can be summarized as follows:

(i) Vacancies in various sublattices (Vc_{Co}, Vc_{Ti}, and Vc_Z). Those appearing in the Co sublattice are found to have the smallest formation energy, its values even turning negative for Co-poor conditions in Co_2TiGe and Co_2TiSn. The Vc_{Ti} and Vc_Z point defects have a significantly larger formation energy, whereby, in each system, the most stable sublattice is the one consisting of Z atoms. A similar trend was also observed in Co_2MnSi by Hülsen *et al.* [53], albeit with a somehow larger value, $\simeq 1$ eV, for $\Delta E[Co_2TiZ, Vc_{Co}]$, which represents the upper bound ($\Delta\mu_{Co} = 0$) of $E_{form}[Vc_{Co}]$. Experiments on Co_2MnZ, on the other hand [54], while confirming vacancy concentrations as high as 2%, suggest a rather random distribution over the lattice sites. An ever increasing Vc_{Co} concentration was found to lead to an $L2_1 \rightarrow C1_b$ ordering transition in $Ni_{2-x}MnSb$ Heusler alloys [55]. A similar scenario may also occur in $Co_2TiSi \rightarrow$ CoTiSi($C23$) and $Co_2TiGe \rightarrow$ CoTiGe($C22$), where the compounds in the 1:1:1 stoichiometry set the lower bound for $\Delta\mu_{Co}$ and thus correspond to small (negative for Z = Ge) defect formation energies for the Vc_{Co} vacancies. An apparently different situation is found in Co_2TiSn, for which we found the CoTiSn ground state to be the $C1_b$ structure but lying outside the Co_2TiSn stability range. Investigations performed by Nobata *et al.* [56] found, on the other hand, that certain growth conditions favor the formation of the $Co_{1.50}TiSn$ with a half-filled vacancy sublattice instead of the stoichiometric compound CoTiSn. This way, the obtained negative formation energy of Co_2TiSn:Vc_{Co} is consistent with the experimental findings. We do emphasize, however, that all the calculated defect formation energies correspond to the limiting case of zero pressure and temperature.

(ii) Co antisites (Co_{Ti} and Co_Z). Following the sequence Si → Ge → Sn, opposite trends can be recognized in the two reference energies $\Delta E(Co_2TiZ, Co_{Ti})$ and $\Delta E(Co_2TiZ, Co_Z)$ that correspond to the two Co antisites. While the former increases with the atomic number of the Z atom, and thus with the lattice constant of the Co_2TiZ compound, the latter decreases. Accounting, however, for the allowed variations in the reduced chemical potentials, which enter as $(-\Delta\mu_{Co} + \Delta\mu_{Ti/Z})$, the two formation energies $E_{form}[Co_{Ti}]$ and $E_{form}[Co_Z]$ are found to be of comparable size for a given system Co_2TiZ. This indicates that both antisites may appear with roughly equal probability during the sample preparation.

(iii) Ti antisites (Ti_{Co} and Ti_Z). Similarly to the previous case, the reference energy of the Ti_Z antisite exhibits a strong dependence on the Z atom, but with an even more significant drop for the heavier elements. As seen in Table II,

TABLE II. Formation energy E_{form} for the native defects in Co_2TiZ (Z = Si, Ge, Sn), calculated using 128-atom supercells within the pseudopotential plane-wave method. The formation energy entries, derived from Eq. (4), are given as an interval $(E^{min}_{form}, E^{max}_{form})$ corresponding to the lower and upper bounds of the chemical potentials $\Delta\mu_\alpha$ and/or their combinations. Also listed are the reference values $\Delta E(Co_2TiZ, D)$ defined by Eq. (5). For the stoichiometric defects A $\leftrightarrow$ B all these quantities are equal.

	$\Delta E(Co_2TiZ, D) \rightarrow (E^{min}_{form}, E^{max}_{form})$ [eV]		
Defect D	Co_2TiSi	Co_2TiGe	Co_2TiSn
Vc_{Co}	0.29 $\rightarrow$ (0.09, 0.24)	0.01 $\rightarrow$ (−0.17, 0.01)	0.28 $\rightarrow$ (−0.08, 0.28)
Vc_{Ti}	2.20 $\rightarrow$ (0.98, 2.15)	2.16 $\rightarrow$ (0.56, 1.55)	2.37 $\rightarrow$ (1.10, 1.91)
Vc_Z	3.21 $\rightarrow$ (1.63, 2.21)	2.87 $\rightarrow$ (1.83, 2.52)	2.96 $\rightarrow$ (2.43, 2.96)
Co_{Ti}	1.90 $\rightarrow$ (0.88, 1.31)	1.96 $\rightarrow$ (0.38, 1.54)	2.16 $\rightarrow$ (0.89, 2.03)
Co_Z	1.90 $\rightarrow$ (0.37, 1.10)	1.37 $\rightarrow$ (0.44, 1.12)	1.20 $\rightarrow$ (0.78, 1.56)
Ti_{Co}	1.21 $\rightarrow$ (1.80, 2.23)	0.85 $\rightarrow$ (1.27, 2.43)	1.00 $\rightarrow$ (1.13, 2.27)
Ti_Z	1.50 $\rightarrow$ (0.86, 1.72)	0.66 $\rightarrow$ (0.29, 1.91)	−0.30 $\rightarrow$ (−0.16, 0.80)
Z_{Co}	2.16 $\rightarrow$ (2.96, 3.69)	2.31 $\rightarrow$ (2.56, 3.24)	3.18 $\rightarrow$ (2.82, 3.60)
Z_{Ti}	0.93 $\rightarrow$ (0.71, 1.57)	1.91 $\rightarrow$ (0.66, 2.28)	2.39 $\rightarrow$ (1.29, 2.25)
Ti $\leftrightarrow$ Co	2.57	2.28	2.63
Ti $\leftrightarrow$ Z	2.18	2.04	1.90
Co $\leftrightarrow$ Z	2.97	2.70	3.21

$\Delta E(Co_2TiSn, Ti_{Sn})$ even becomes negative. One can conclude that, when Ti is in excess, a preference for the Ti_Z antisite should be observed, at the expense of Ti_{Co}. This is quite an opposite trend as the one seen in Co_2MnSi, where the Mn_{Co} antisite was found to have a much smaller reference energy than Mn_{Si} [53]. As a general observation, we emphasize here the fact that the lower/upper boundary for an antisite A_B becomes the upper/lower boundary with opposite sign for its B_A counterpart. Comparing now the two "paired" antisites Ti_{Co} and Co_{Ti}, we note again that the allowed $\Delta\mu_\alpha$ intervals significantly influence the formation energy results. Indeed, whereas $\Delta E(Co_2TiZ, Ti_{Co})$ is about half the size of $\Delta E(Co_2TiZ, Co_{Ti})$, the corresponding E_{form} values have a rather broad overlapping interval, with a lower boundary for the Co_{Ti} antisite.

(iv) Z antisites (Z_{Co} and Z_{Ti}). As could be anticipated from the Vc_Z case, the sublattice formed by the group IV elements appears to be the most stable. The Z_{Co} antisites exhibit by far the largest formation energies and are therefore the least likely to occur. The formation energies obtained for the Z_{Ti} defects are somewhat smaller, but still larger than their Ti_Z correspondents. We further note that the $\Delta E(Co_2TiZ, Z_{Ti})$ values increase along the Si $\rightarrow$ Ge $\rightarrow$ Sn series, in contrast to the trend observed for the Ti_Z antisites.

(v) Swaps (Ti $\leftrightarrow$ Co, Ti $\leftrightarrow$ Z, and Co $\leftrightarrow$ Z). The calculations performed by Picozzi *et al.* [57] for the Co_2MnSi full Heusler alloy found an interesting feature in the formation energy of the Mn $\leftrightarrow$ Co swap: its value closely matches the sum of the reference energies of the Mn_{Co} and Co_{Mn} antisites. Our results do not reproduce this behavior in any of the Co_2TiZ compounds, regardless of the considered swaps. A possible reason may be the large differences between the corresponding reference energies of the paired antisites, which could efficiently curtail the swapping tendencies. As Table II shows, we find very large formation energies for all investigated swaps. These findings appear to be in contradiction with the experimental results obtained for the Co_2TiSn Heusler alloy [43], for which the authors report NMR data indicative of the crystal structure being partially $D0_3$-like, consistent with a Ti $\leftrightarrow$ Co swap.

To conclude, we found several defects in Co_2TiZ to have a quite low formation energy, whereas others, in particular the swaps and those related to the Z-atom sublattice, should occur with reduced probability. Some of the more likely defects have been selected for subsequent investigations concerning the effect they have on the electronic structure and the implications for the transport properties. These results form the subject of the next sections.

IV. DEFECT-TRIGGERED CHANGES IN THE ELECTRONIC STRUCTURE

We present in this section the results obtained employing the FP-SPR-KKR Green function method, modeling the intrinsic defects as dilute alloys. We focus on those systems which were found to have a small formation energy and follow the changes in the electronic structure brought about by the defects, emphasizing specific aspects relevant for the transport properties. In doing so, we use the Bloch spectral function (BSF) [58], expressed as the Fourier transform of the configurationally averaged Green function,

$$A(\vec{k}, E) = -\frac{1}{\pi N}\mathrm{Im}\sum_{m,n}^{N} e^{i\vec{k}(\vec{R}_m - \vec{R}_n)} \times \int d^3r \langle G(\vec{r} + \vec{R}_m, \vec{r} + \vec{R}_n; E)\rangle, \quad (12)$$

performed over N atomic sites with position vectors $\vec{R}_m$ and $\vec{R}_n$ in the crystal lattice. This quantity, which can be seen as a $\vec{k}$-resolved density of states (DOS), is well defined also for ordered systems. In this case the configurational average, symbolized by $\langle \ldots \rangle$, drops out and the evaluation takes place for a complex energy argument $E + i\varepsilon$ with $\varepsilon \rightarrow 0$, providing the ordinary dispersion relation $E_{\vec{k}}$.

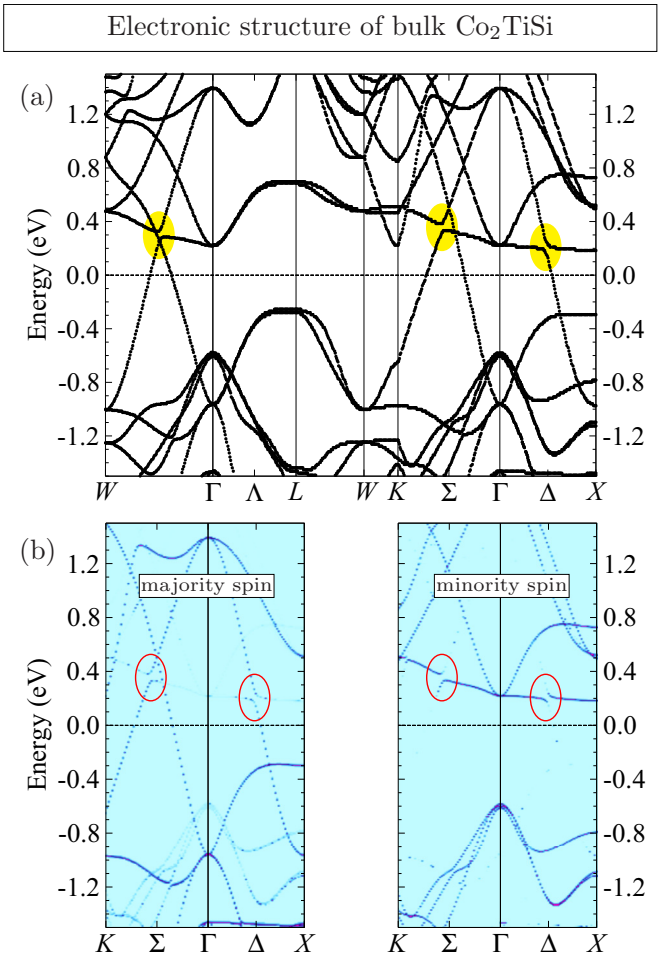

FIG. 4. (a) Spin-polarized relativistic dispersion relation $E_{\vec{k}}$ and (b) spin-resolved BSFs along selected high-symmetry directions in the fcc BZ, calculated for the Co_2TiSi full Heusler alloy in the $L2_1$ structure obtained using the FP-SPR-KKR method. The energy is given relative to the Fermi energy E_F of the system. The highlighted areas located 0.2–0.4 eV above E_F along the W-Γ, K-Γ, and Γ-X directions point to anticrossings between a Co majority-d and a Co minority-d band, which occur as a result of spin-orbit coupling.

Taking the Co_2TiSi full Heusler alloy as an illustrative example, we present the BSFs for a series of dilute alloys modeling the Co_2TiSi:D defects. Calculated on a fully relativistic level, the BSFs are subsequently projected on their spin components and compared with the standard band structure of the parent compound. This allows us to identify signatures of the defect-induced minority-spin impurity bands in the proximity of the half-metallic gap. We will also show that, owing to the SOC, a majority-spin d band that crosses the Fermi energy E_F gains minority-spin character. This rather ubiquitous effect is larger for the Co-related defects Vc_{Co} and Co_{Si}, significantly reducing the spin polarization near E_F.

A. Results for Co_2TiSi bulk

The spin-polarized relativistic electronic structure for the ordered compound Co_2TiSi is displayed in Fig. 4, with panel (a) depicting the calculated dispersion relation along several high-symmetry directions in the fcc BZ and panel (b) the corresponding spin-resolved BSF obtained for an imaginary part of the energy $\varepsilon = 0.005$ Ry along the K-Γ-X path of the BZ. The spin-resolved results of Fig. 4(b), consistent with previously reported band structure calculations on a scalar relativistic level [20,22], demonstrate the half-metallic character of this system. The Fermi energy E_F, taken here as the energy reference, is seen to lie close to the upper edge of the band gap appearing in the minority-spin channel.

Of particular interest for the transport properties, in general, and for the Seebeck coefficient in particular, are the states located in the proximity of E_F, according to Eq. (8). As seen in Fig. 4(a), there are only two bands that cross the Fermi energy. Starting from 1.4 eV at the Γ point, one band goes down in energy and gets below E_F at the X and W points. It thus leads to a Fermi surface enclosing the Γ point and forming pockets at the BZ edge. The second band rises in energy from −1.0 eV at the Γ point and forms a Fermi surface connecting to adjacent BZs. Stemming from the Co d orbitals, these two bands possess a dominant majority-spin character, as revealed by the BSF shown in Fig. 4(b), and are expected to dominate the transport properties in these compounds. A much flatter Co d band is found slightly above the Fermi energy, forming the minority-spin conduction band. Its minimum lies at the X point of the BZ, such that the half-metallic gap, as seen on the right side of Fig. 4(b), is indirect. We note here that although the isoelectronic compounds Co_2TiGe and Co_2TiSn exhibit qualitatively similar results, one does find quantitative variations in both the width of the half-metallic gap and the position of the Fermi energy inside it. For the former, the FP-SPR-KKR calculations give 0.76, 0.57, and 0.48 eV, respectively, for $Z =$ Si, Ge, and Sn. Measured relative to E_F, the minority-spin conduction band minimum, on the other hand, was found at 0.18, 0.21, and 0.26 eV.

Highlighted in Fig. 4 are several areas along the W-Γ, K-Γ, and Γ-X directions where this minority-spin d band intersects the two majority-spin d bands, in a range of 0.2–0.4 eV above E_F. Qualitative differences in these intersections are easily recognizable: The falling majority-spin band has the same parity (and symmetry) as the minority-spin band, which leads to an *anticrossing* between the two bands. In turn, the other majority-spin band rising from the Γ point crosses the minority-spin band without coupling to it, as seen along the W-Γ and K-Γ directions.

The repelling of the two bands of different spin character is caused by SOC. By virtue of a mechanism suggested by Mavropoulos *et al.* [59] when discussing the effect of spin-orbit coupling on the band gap of half metals, the coupling of the two bands causes a strong spin mixing. Regarding the SOC as a perturbation to the spin-dependent crystal Hamiltonian with eigenvalues $E^{\uparrow}(\vec{k})$ and $E^{\downarrow}(\vec{k})$, the potential terms causing the spins to flip are proportional, in leading order, to $1/[E^{\uparrow}(\vec{k}) - E^{\downarrow}(\vec{k})]$. It becomes apparent that the spin mixing will exhibit a maximum where the unperturbed spin-up and spin-down bands would cross. Indeed, as evidenced in Fig. 4(b), the BSF of a given spin character (here obtained within a Dirac formalism) is an "image" of the opposite spin over a broad range around the anticrossing points. This effectively leads to a reduced spin polarization especially at the top edge of the half-metallic gap [59], since the states in its vicinity no longer possess a unique spin character. We note

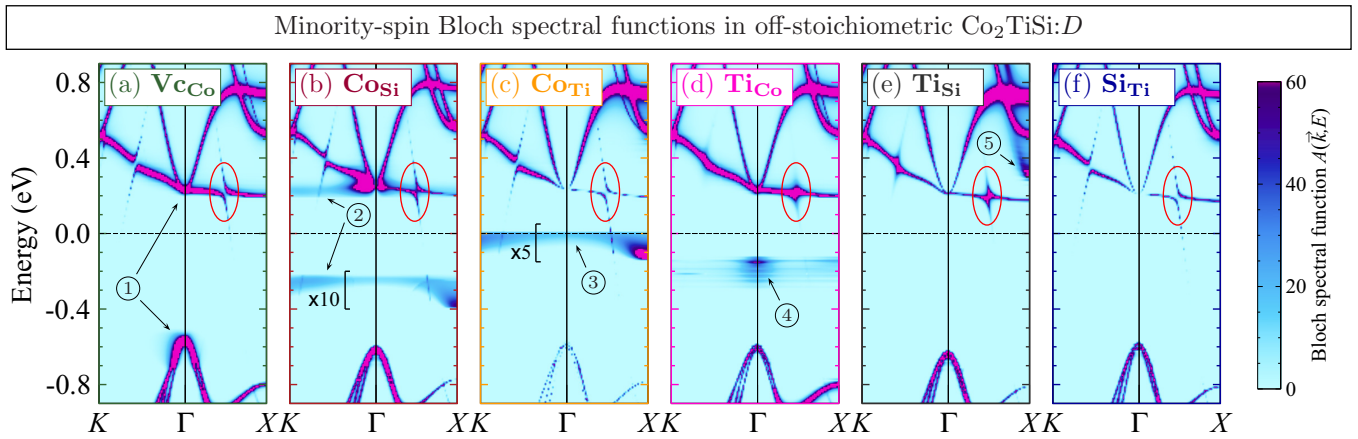

FIG. 5. Minority-spin BSFs along the K-Γ-X direction in the fcc BZ, calculated for several off-stoichiometric native defects in Co_2TiSi modeled as dilute alloys with 3 at. % defect composition. The energy scale is given relative to the Fermi energy of each system.

that a similar imaging effect occurs below the Fermi energy around the Γ point. As can be seen in Fig. 4(b), one finds a set of valence bands that exhibit finite amplitudes of the BSF in both spin channels. The reason for spin mixing in this case is related to the intra-atomic SOC, with the states originating from d orbitals with large magnetic quantum numbers, $\pm 5/2$ and $\pm 3/2$.

B. Spectral function of dilute alloys

We have selected, from the list of all possible intrinsic defects investigated above, a total of six systems, exhibiting low formation energies. According to the results presented in Table II, these are as follows: vacancies on Co sublattice Vc_{Co}, the Co antisites Co_Z and Co_{Ti}, the Ti antisites Ti_{Co} and Ti_Z, and the Si antisite Z_{Ti}. We employed a dilute alloy modeling for all these systems, as described in Sec. II C, by considering a defect of type D_A as a single-site effective medium ($A_{1-x}D_x$) while keeping the other sublattices unchanged. Without loss of generality, the discussion below is restricted to the Co_2TiSi:D systems (Z = Si) with $x = 0.03$, corresponding to a single defect in the 128-atom supercell used in the formation energy calculations.

Our primary interest is to investigate the changes in the electronic structure occurring in the proximity of the Fermi energy. As shown above, only two bands do cross E_F, both having a dominant majority-spin character. For this spin channel we found that while the BSFs associated with these bands may differ quantitatively from one system to another, no qualitative deviations occur, irrespective of the group IV element Z and the type of defect. We shall therefore focus in the following on the minority-spin BSFs in a $\simeq 2$ eV energy window around E_F, with emphasis on two aspects: (i) the defect-induced states evolving in impurity bands (IBs) near the half-metallic gap, and (ii) the so far unexplored effect of the defects on the SOC-induced band anticrossings observed for the ordered compound.

The minority-spin BSFs for the off-stoichiometric Co_2TiSi:D systems are shown in Fig. 5. Note that, while choosing the same K-Γ-X direction in the BZ as for the Co_2TiSi BSFs in Fig. 4(b), for clarity purposes the energy interval around the Fermi energy E_F has been reduced. Moreover, since we are dealing now with an alloy system, Eq. (12) is evaluated for real energy arguments and the broadening of the alloy bands is due to the intrinsic disorder of the CPA effective medium. We first analyze, on the basis of Fig. 5, the defect-related states appearing in the investigated systems, appropriately labeled from (1) to (5) in each panel.

(1) Vacancies in the Co sublattice, Fig. 5(a), induce minority-spin states at the edges of the half-metallic gap, thus reducing its width and, consequently, the size of the spin gap. The latter is defined as the minimum energy required to flip the electron spin. The side-by-side comparison of the different panels of Fig. 5 reveals that the highest minority-spin valence band maximum is obtained for Co_2TiSi:Vc_{Co}. Actually, within a broad range around the Γ point the minority-spin BSF of this system is characterized by a much stronger intensity as compared to the other alloys. These results are consistent with those obtained by Özdoğan *et al.* [60] for various Co-based Heusler alloys from the series Co_2(Mn,Cr)(Al,Si). Similarly to these systems, we find that although the presence of Co vacancies reduces the total magnetization (e.g., from 2.00 to 1.90 μ_B per formula unit in the case of 3% vacancy concentration in Co_2TiSi), the half-metallicity is not destroyed. Because of the large value of the spin gap, we expect the half-metallicity to be quite robust against Co-vacancy formation, at reasonably low concentrations, in all Co_2TiZ compounds.

(2) The Co_{Si} antisite, Fig. 5(b), creates two minority-spin IBs near the Fermi energy. These are distributed rather symmetrically below and above E_F, centered around -0.3 and 0.2 eV, respectively. Thus, the lower band falls inside the half-metallic gap, whereas the higher one overlaps with the edge of the minority-spin conduction band. In spite of the IB present in the gap, the Co_2TiSi:Co_{Si} also remains half metallic. As further indicated in Fig. 5(b), the BSF has been multiplied by a factor 10 in the energy interval $[-0.4, -0.2]$ eV for all $\vec{k}$ vectors, a value that represents the relative weight of the DOS associated with the high and low IBs. Although running rather parallel to each other, these two bands differ qualitatively in their dependence on $\vec{k}$. While the upper IB has a large weight near the Γ point, enhancing and significantly broadening the BSF, the low one exhibits a maximum near the X point, at the edges of the BZ.

(3) The Co_{Ti} antisite, Fig. 5(c), creates a single IB in the energy region of interest. Located inside the half-metallic gap, this band is nearly touching the Fermi level, such that the $Co_2TiSi:Co_{Ti}$ system is predicted to loose its half-metallic character. A comparison with the low Co_{Si}-IB reveals qualitatively similar $\vec{k}$ distributions in the BSF, with the amplitude increased far away from the Γ point. The two cases are, however, quantitatively substantially different. As indicated by the different multiplicative factors applied, the Co_{Ti}-BSF amplitude is about twice as large as compared to the Co_{Si} one. One further notes, in addition, the much weaker broadening of the BSFs in this system, with the alloy bands largely preserving their bulk character.

The features related to the Co antisites discussed here are in very good agreement, both in their energy position and in their amplitude, to those reported in the literature for other Co-based full Heusler alloys such as Co_2MnSi [53,57], Co_2MnGe [57], Co_2CrAl [61], and Co_2VSn [62].

(4) Another IB falling inside the half-metallic gap is the one related to the Ti_{Co} antisite, shown in Fig. 5(d). One notes that, compared to the previously surveyed IBs, this has the highest intensity, no up-scaling having been applied in this panel. It is located $\simeq 0.2$ eV below E_F, thus bearing no influence on the half-metallicity of the system and, in contrast to the previous ones, is strongly peaked around the BZ center.

(5) Finally, the signature of a Ti_{Si}-related IB can be seen in Fig. 5(e) in the vicinity of the X point, at $\simeq 0.3$ eV above the Fermi energy. It is close to and eventually merges into a band complex stemming from the d orbitals of the Ti sublattice. Owing to its location, this IB has no direct influence either on the half-metallic or on the transport properties of the system.

Highlighted by red ellipses in Fig. 5 are the spin-mixing d-d band anticrossings which lie in the vicinity of the Fermi energy. We focus on the minority-spin image of the falling majority-spin band. Its spectral function shows variations from system to system, with the SOC-mediated spin-mixing effect strongly depending on the defect type. The Vc_{Co} and Co_{Si} defects are characterized by a continuous BSF with large values extending deep into the half-metallic gap. For the Ti-sublattice-related defects Co_{Ti} and Si_{Ti}, the amplitude of spin mixing is smaller and the BSF exhibits merely a discrete rather than a continuous character. In the case of the Ti_{Co} and Ti_{Si} antisites, the flat Co band preserves almost completely its minority-spin character. The band repulsion is very weak and large BSF values are found only in a small energy interval around the anticrossing point.

The most important observation to be made at this point concerns the possible changes in conductivity that may result from these anticrossings. This is because the two alloy bands involved differ not only in their dominant spin character, but also in their associated Fermi velocity. One can think of a defect creating additional minority-spin states in the appropriate energy range. As a result of the spin mixing, these states will not only gain majority-spin character; but they will also *borrow the dispersion* of the band with which they mix. A direct consequence, shown below to occur in the two systems containing Vc_{Co} and Co_Z, is an increased conductivity in the energy range near the band mixing.

We close this section with a brief comment on the dependence of the discussed effects on the group IV element

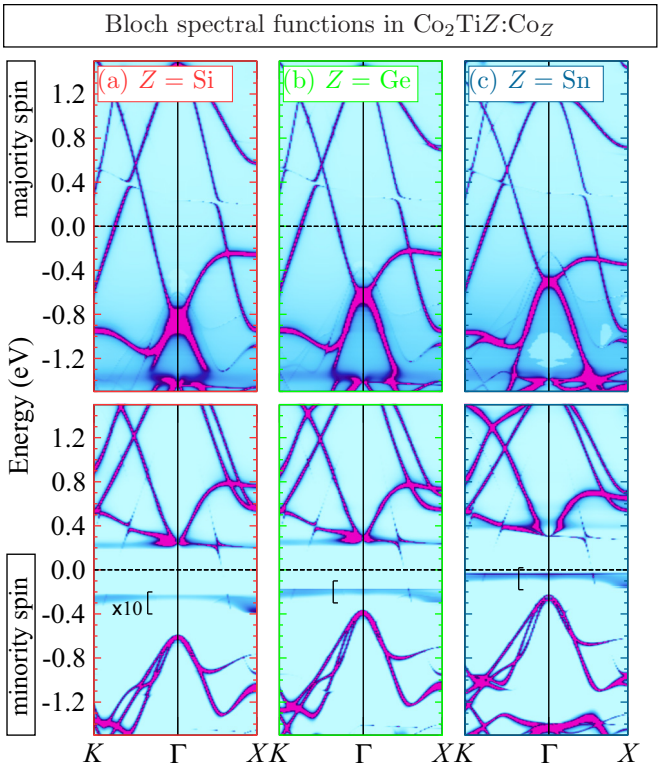

FIG. 6. Spin-resolved BSFs for the $Co_2TiZ_{0.97}Co_{0.03}$ alloys modeling the Co_Z antisite, with Z = Si, Ge, and Sn corresponding to panels (a), (b), and (c). In each panel, the minority spin BSF has been multiplied by a factor of 10 in a 0.2 eV interval around the lower IB.

Z in the Co_2TiZ series. Taking as an example the Co_Z antisite system modeled as $Co_2Ti(Z_{0.97}Co_{0.03})$, we show in Fig. 6 the BSFs of the three different alloys for both spin components.

The majority-spin states (top panel) close to the Fermi energy do not vary too much when changing the Z atom. A slight upward shift of the valence bands can be noted upon increasing the atomic number from Si to Sn. It originates from hybridization between the Co d and the Z p states which occurs already in the ordered compounds [22,42], and is manifesting itself in both spin channels. Indeed, as seen in the bottom panel of Fig. 6, also the minority-spin d bands are found at higher energies in $Co_2TiSn:Co_{Sn}$ as compared to $Co_2TiSi:Co_{Si}$. The effect is more pronounced in the valence band, leading to a monotonic reduction of the half-metallic gap in the series Si → Ge → Sn. The two IBs related to the Co_Z antisite follow a similar upwards shift while maintaining a nearly constant separation. The striking resemblance of the minority-spin BSFs in the Si- and Ge-based systems should be noted here, while $Co_2TiSn:Co_{Sn}$ exhibits qualitative differences. On one hand, the low IB approaches the Fermi energy, thus strongly reducing its half-metallic character. The upper IB, on the other hand, moves above the Co d band at 0.3 eV, with a subsequent strong reduction of the BSF around the Γ point.

V. INFLUENCE OF DEFECTS ON THE TRANSPORT PROPERTIES

This section presents the calculated transport properties of the $Co_2TiZ:D$ systems, obtained by employing the CPA-based

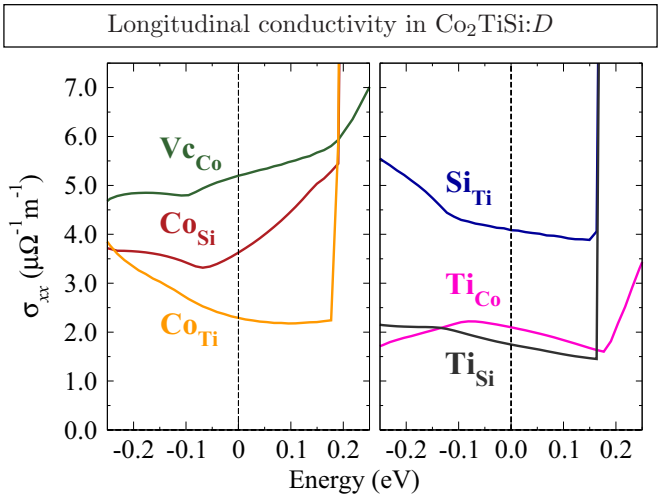

FIG. 7. Energy dependence of the diagonal element $\sigma_{xx}(E)$ of the electronic conductivity tensor, calculated for the same off-stoichiometric native defects in Co_2TiSi as those shown in Fig. 1.

dilute alloy modeling. We start with a detailed analysis of the series of Co_2TiSi:D systems with 3% defect concentration surveyed in the previous section. The results obtained for the energy-dependent electronic conductivity are used to interpret the calculated Seebeck coefficient, shown in Fig. 1. The connection of both quantities with the particular features of the underlying electronic structure will be appropriately shown. Our discussion will then be extended by covering different defect concentrations and all the group IV elements Z in Co_2TiZ:D. We show that the conclusions derived from the Co_2TiSi:D systems are of general validity in the dilute limit, with the Seebeck coefficient exhibiting only a weak dependence on both factors.

A. Electronic conductivity in Co_2TiSi:D

The calculated energy-dependent electronic conductivity of the Co_2TiSi:D dilute alloys is shown in Fig. 7. We only plot the longitudinal $\sigma_{xx}(E)$, given relative to the Fermi energy E_F of each system (dashed vertical line). Indeed, we found that, over a broad energy range, $E_F \pm 0.1$ eV, the difference $\sigma_{zz}(E) - \sigma_{xx}(E)$, a measure for the anisotropic magnetoresistance (AMR), does not exceed 1% for all the investigated systems.

The results of our calculations indicate a strong variation of the residual conductivity $\sigma_{xx}(E = E_F)$ with the type of defect, with values ranging from 1.75 $\mu\Omega^{-1}$ m^{-1} for Ti_{Si} to 5.20 $\mu\Omega^{-1}$ m^{-1} for Vc_{Co} at 3% defect concentration. All these values are higher than the 0.45 $\mu\Omega^{-1}$ m^{-1} deduced from the experimentally reported residual resistivity [20], indicating additional sources of carrier scattering in the samples. Consistent with the decrease of $\sigma_{xx}(E = E_F)$ with defect composition observed in our calculations, these could be point defects in high concentration and/or other crystal imperfections. Analogous results were obtained also for Co_2TiGe:D and Co_2TiSn:D. These defect-dependent *quantitative* differences directly reflect the changes occurring in the majority-spin bands that cross the Fermi energy. Qualitatively, while a smooth dependence of all $\sigma_{xx}(E)$ curves in the $E_F \pm 0.15$ eV energy interval is obvious, several peculiarities can be noted: (i) in four cases the conductivity dependence on its energy argument exhibits a negative slope around E_F; (ii) a steep increase of $\sigma_{xx}(E)$ occurs at energies above $\simeq 0.18$ eV; (iii) in two of the investigated systems, $Co_2TiSi:Vc_{Co}$ and $Co_2TiSi:Co_{Si}$, the conductivity is characterized by a *positive* slope around the Fermi energy. The reasons for these qualitative differences are discussed in detail in the following:

(i) The negative slope in the energy dependence of $\sigma_{ii}(E)$ around E_F obtained in the case of Co_{Ti}, Si_{Ti}, Ti_{Co}, and Ti_{Si} defects is similar to that found in the bulk Co_2TiZ systems [16,20]. Indeed, for all these materials the DOS decreases above E_F such that, in the approximation of an energy-independent scattering, the conductivity is expected to decrease with increasing energy E. One can then conclude that, at least in a range extending not far away from the Fermi energy, the presence of these four defects leads to a weak, nearly energy-independent scattering of the electrons. This generic behavior can be modified, however, if IBs are present. This is the case for the Ti_{Co} antisite, where the IB found below E_F [labeled (4) in Fig. 5(d)] adds a hole-like contribution to the conductivity. The $\sigma_{xx}(E)$ curve for this system (right panel of Fig. 7) exhibits a peak below the Fermi energy, not seen, for example, in the Ti_{Si} case. Let us note that no evidence was found for contributions to $\sigma_{ii}(E)$ in the case of Co_{Si} or Co_{Ti} IBs lying below E_F.

(ii) The strong increase in $\sigma_{ii}(E)$ at higher energies, $\simeq 0.18$ above E_F, is caused by the onset of the minority-spin conduction band stemming from the Co d orbitals. The rise to a plateau of 12–14 $\mu\Omega^{-1}$ m^{-1} appears as an abrupt jump due to the chosen scale of the figure. One has to note here that we have purposefully chosen a narrow interval for displaying $\sigma_{xx}(E)$ in order to emphasize its E dependence around E_F. We have checked the results against numerical stability in the E range around the rising point by refining the BZ integration for a $\vec{k}$ mesh as high as 6×10^6 points and found no smoothening in $\sigma_{xx}(E)$. Moreover, the calculated $\sigma_{xx}(E)$ values correspond to $T = 0$ K such that, at any finite temperature, the sharp steps will be washed out. For two of the systems, containing the Vc_{Co} and Ti_{Co} defects, the $\sigma_{xx}(E)$ increase is less abrupt. In these cases the minority-spin Co band, stemming from the perturbed sublattice, is effectively broadened as a result of alloying. Moreover, the presence of the impurity on a single Co sublattice [see Fig. 2(b)] destroys the inversion symmetry of the host crystal. Under this condition, SOC leads to scattering between states that are no longer degenerate, increasing the magnitude of the energy-dependent scattering.

(iii) In contrast to the situation above, the positive slope of $\sigma_{xx}(E)$ near E_F observed for the $Co_2TiSi:Vc_{Co}$ and $Co_2TiSi:Co_{Si}$ indicates a strong energy-dependent scattering occurring in these systems. Following the inversion symmetry suppression in the former and the presence of a strong impurity band in the latter, the electronic conductivity increases right above E_F. In both cases we suggest that a SOC-mediated broadening and redistribution of states taking place around the anticrossing points is responsible for the observed effect. As pointed out above in the BSF analysis, the additionally created minority-spin states may *borrow mobility*, via spin mixing, from the majority-spin bands.

B. Seebeck coefficient in Co_2TiSi:D

By virtue of Eqs. (8) and (9), the Seebeck coefficient $S(T)$ is expressed as the quotient of the first and zeroth moments of the conductivity. The findings related to the changes in the energy dependence of $\sigma_{ii}(E)$ can then be directly transferred to the corresponding results obtained for $S(T)$ presented above in Fig. 1. One can easily understand the broad range of values, varying both in sign and magnitude, obtained for the different kinds of defects as arising from variations in either $L_{ii}^{(0)}$ (denominator) or $L_{ii}^{(1)}$ (numerator).

Assuming an energy-independent scattering, our theoretical results predict a positive Seebeck coefficient for the bulk Co_2TiZ materials [16,20], a finding which is in contrast to the large, negative values reported experimentally, reaching as much as $-30\ \mu$V/K in Co_2TiSi/Ge and $-50\ \mu$V/K in Co_2TiSn [20,23].

As seen in Fig. 1, this tendency of a positive Seebeck coefficient is retained for the systems that have a weakly energy-dependent scattering, such as Co_{Ti}, Ti_{Co}, Si_{Ti}, and Ti_{Si}. As the temperature increases, the contribution of the minority-spin electrons becomes more important. This is because the minority-spin bands above the half-metallic gap become populated at higher temperatures. As shown above, in the case of defects with a weakly energy-dependent scattering the onset of conductivity in the minority-spin bands leads to an abrupt rise in the conductivity and thus to a negative, electron-like contribution to the Seebeck coefficient. As a result, the Seebeck coefficient drops sharply and becomes negative at elevated temperatures for the systems containing Co_{Ti}, Si_{Ti}, and Ti_{Si}. One notes here the direct relation between the change of slope for $S(T)$ and the ever increasing contribution coming from the flat minority-spin band. The exception to this behavior is represented by the Ti_{Co} antisite where the presence of the IB below E_F was shown to add a hole-like contribution to the conductivity, a contribution which is large enough such as to preserve a positive Seebeck coefficient throughout the whole investigated temperature range.

In the systems with a strong energy-dependent scattering, the conductivity was found to be larger above E_F than below. This leads to a negative Seebeck coefficient, as obtained for Co_2TiSi:Vc_{Co} and Co_2TiSi:Co_{Si}. We note that only in these cases the results qualitatively reproduce the experimentally observed behavior. For the Co_{Si} antisite the calculated $S(T)$ deviates within 30% from the experimental data for $T \leqslant 300$ K. As we will show below, only varying the defect concentration is not sufficient to further improve the agreement between our calculations and experiment, which is particularly deteriorating at higher temperatures. Indeed, it is expected that spin fluctuations (not accounted for here) become important when the Curie temperature is approached, and that magnon drag effects will lead to an enhanced thermopower. We note that, within a hydrodynamic theory of such effects, the sign of the Seebeck coefficient obtained from an independent-electron calculation is preserved [63].

C. Effect of defect concentration and of group IV element

We have established so far the needed link between the electronic structure and, through the energy dependence of the electronic conductivity, the main features of the Seebeck coefficient in the Co_2TiSi:D systems. We now extend our analysis to a broader quantitative level by investigating two effects: (i) a varying defect concentration, and (ii) different group IV element in the Co_2TiZ:D series.

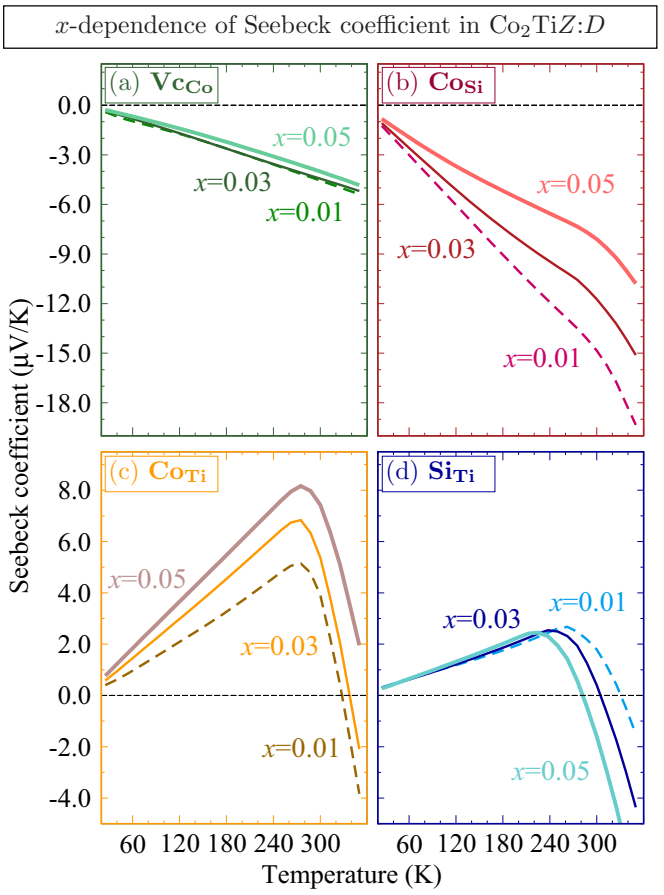

FIG. 8. Seebeck coefficient $S(T)$ calculated for several off-stoichiometric native defects in Co_2TiSi:D. With each defect D_A modeled as a single-site effective medium $A_{1-x}D_x$, the dashed, thin solid, and thick solid lines correspond to $x = 0.01$, $x = 0.03$, and $x = 0.05$, respectively. Panels in the same row have identical scales for $S(T)$.

Figure 8 shows the calculated temperature-dependent Seebeck coefficient $S(T)$ for three different off-stoichiometric compositions $x = 0.01$, $x = 0.03$, and $x = 0.05$. Due to their fairly similar behavior to that of the Co_{Ti} system, the corresponding Ti antisite-related curves Ti_{Co} and Ti_{Si} have been omitted in this figure.

We start by noting that a monotonic decrease of $\sigma_{ii}(E)$ as a function of defect composition was observed for all investigated systems. Accordingly reflected in the integrated quantities defined by Eq. (8), $L_{ii}^{(0)}$ decreases with x irrespective of the defect considered. The differences in the $S(T)$ concentration dependence noticed in Fig. 8, weak for Vc_{Co} and Si_{Ti} and rather pronounced for Co_{Ti} and Co_{Si}, can be related to the behavior of the $L_{ii}^{(1)}$ term, measuring the *asymmetry* of $\sigma_{ii}(E)$ about the Fermi energy.

Indeed, if this term remained constant with x, one would obtain a monotonic increase in the absolute value of the

Seebeck coefficient, $|S(T)|$, which is obviously the case for the Co_{Ti} defect, panel (c) of Fig. 8. For Vc_{Co} and Si_{Ti} [panels (a) and (d)] the nearly concentration-independent $S(T)$ indicates an asymmetry term that decreases with x, without changing its sign, thus compensating the decrease of $L_{ii}^{(0)}$. Note that in the case of Si_{Ti}, the shift of the $S(T)$ peak is caused by a slight upward shift in the Fermi energy taking place with increasing Si content. An even faster decrease of $L_{ii}^{(1)}$ was found to occur for the Co_{Si} system [panel (c)]. All these cases can be understood as a consequence of a broadening and smoothening, with increasing concentration x, of the additional contributions to $\sigma_{ii}(E)$ from above E_F.

Analogous considerations can be applied when analyzing the dependence of the Seebeck coefficient on the group IV element Z in the isoelectronic systems $Co_2TiZ{:}D$. The corresponding results for all investigated defects at a net composition of $x = 0.03$ are shown in Fig. 9.

Although the conductivity is mainly dominated by majority-spin carriers, one can ascribe the various differences in the Z-atom dependence of $S(T)$ as being mostly related to changes occurring in the minority-spin channel. Indeed, the BSFs displayed in Fig. 6 for the $Co_2TiZ{:}Co_{Si}$ system hint at a nearly unchanged majority-spin DOS around E_F for all three systems with Z = Si, Ge, and Sn. Yet there is no simple rule, applicable to all defects, that would explain how $\sigma_{ii}(E)$ depends on the atom Z of the host material. The lack of such a rule is reflected in the Seebeck coefficient being the largest in $Co_2TiSi{:}Ti_{Si}$ for the Ti_Z antisite [panel (e) of Fig. 9] and the smallest in $Co_2TiSi{:}Si_{Ti}$ for Z_{Ti} [panel (f)].

We have previously identified three systems, Co_{Ti}, Ti_Z, and Z_{Ti}, which are characterized by a sudden change of slope in $S(T)$ at elevated temperatures. This behavior was associated with the minority-spin bands above the half-metallic gap becoming populated with increasing temperature. As the offset of these bands relative to E_F increases with Z (see Fig. 6), the peak in $S(T)$ also shifts towards higher T values when Z changes from Si to Ge and then Sn.

The absence of such a peak in $Co_2TiSi{:}Ti_{Co}$ was shown to be caused by the IB present 0.1 eV below E_F, states introducing a rather large hole-like contribution to the conduction. A similar IB is present in all $Co_2TiZ{:}Ti_{Co}$ systems, with its relative position inside the half-metallic gap remaining fairly the same.

For the two defects for which the Seebeck coefficient had a negative sign, $Co_2TiSi{:}Vc_{Co}$ and $Co_2TiSi{:}Co_{Si}$, we find this sign to persist for Co_2TiGe and Co_2TiSn. Moreover, we note that for both defects $|S(T)|$ *increases* with increasing atomic number of the group IV element Z, a rather nonintuitive behavior. Indeed, the calculated $\sigma_{ii}(E)$, which is governing the size of $L_{ii}^{(0)}$, also increases monotonically along the series Si → Ge → Sn. It follows that the increase in $|S(T)|$ can only be accounted for by a much larger increase in $L_{ii}^{(1)}$, the asymmetry term. Noting that the SOC strength also increases as moving down in the group IV, we conclude that the obtained results are consistent with the interpretation given about the role of the SOC in causing a largely asymmetric conductivity. It consists of a redistribution of states in the systems lacking inversion symmetry (as in $Co_2TiZ{:}Vc_{Co}$) and an increased mobility of the minority-spin IB by mixing it with the majority-spin band crossing the Fermi energy, in $Co_2TiZ{:}Co_Z$.

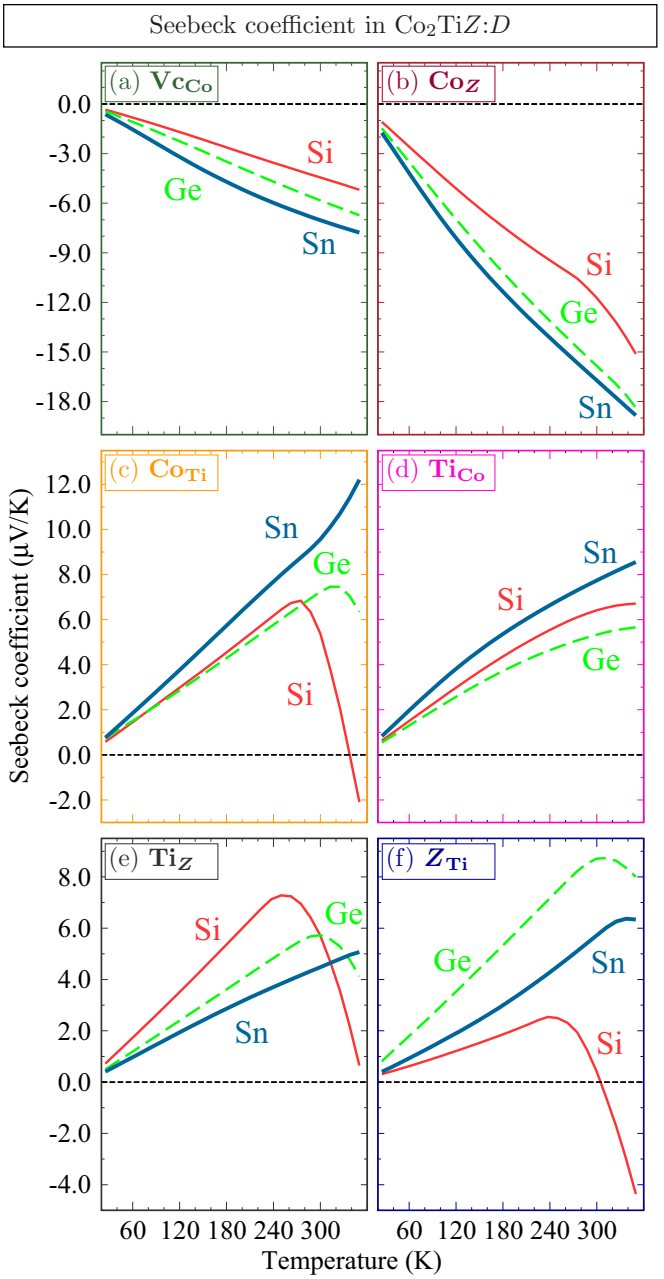

FIG. 9. Seebeck coefficient $S(T)$ calculated for the selected defects in $Co_2TiZ{:}D$ at 3% defect composition. In each panel, the curves corresponding to different group IV elements Z are represented by the (red) thin solid, (green) long dashed, and (blue) thick solid lines for Si, Ge, and Sn, respectively. Panels in the same row have identical scales for $S(T)$.

VI. CONCLUSIONS

The Ti-based Heusler alloys Co_2TiZ (Z = Si, Ge, Sn) have been studied by means of density-functional calculations with the goal of exploring their suitability for spintronics and spin-caloric applications. Since the ideal Heusler alloys of this composition are ferromagnetic half metals, it is of

particular interest to learn how the half metallicity is modified in realistic materials, including off-stoichiometry and atomic-scale disorder. To this end, the formation energies E_{form} of intrinsic point defects have been calculated, and their consequences for electronic transport and thermopower have been explored.

While the formation of antistructure defect pairs by atomic swaps is generally found to be energetically costly, our calculations indicate a very high sensitivity of the ternary Heusler alloys to deviations from their ideal stoichiometry. Once formed in appreciable numbers, point defects caused by off-stoichiometry significantly influence the electrical conductivity. Moreover, the Seebeck coefficient turns out to be a sensitive probe for the presence of defects, even in the simple situation treated here, of single defect formation, rather than interacting pairs.

The lowest values of E_{form} are found for Vc_{Co} and Ti_Z, followed by the Co-related antisites Co_{Ti} and Co_Z. The formation energy of Ti_Z may become negative in the case of $Z = \text{Sn}$, and is still small in the Si and Ge compounds (0.48 eV and 0.30 eV, respectively). Under Co-deficient conditions, the formation energy of Vc_{Co} may become negative for the Ge and Sn-based alloys, indicating that Co vacancies may occur spontaneously. Intrinsic point defects are to be expected also under Co-rich conditions, since E_{form} of Co_Z and of Co_{Ti} are fairly low (in the 0.3 to 0.6 eV range) for Heusler alloys containing Si or Ge, while being somewhat higher in Co_2TiSn. Hence, anything that comes close to ideal Heusler alloys can be synthesized only under very special conditions when the stoichiometry is met exactly, since slight deviations from stoichiometry, both to the Co-rich or the Co-poor side, are likely to lead to point defect formation. Further support for the abundance of defects comes from measurements of the electrical conductivity, where a high residual resistivity, and only a moderate increase (in the range of 30% to 50%) from low to room temperature, have been observed experimentally [20]. This points to a relatively high concentration of native defects in the material, formed already during sample preparation.

While one would expect from the density of states at the Fermi energy a positive Seebeck coefficient in all three alloys, experiments reported negative values throughout the whole temperature range [20,23]. In this context, it is important that our calculations of electronic transport demonstrate a strong effect of point defects on the thermopower of the $\text{Co}_2\text{Ti}Z$ Heusler alloys. At defect concentrations of a few percent, the results obtained here indicate that the magnetic order and the half metallicity in these materials is largely retained. Hence, the majority-spin carriers dominate the electronic transport, ruling out earlier explanations of the negative Seebeck coefficient being due to a breakdown of magnetism and a nonmagnetic electronic structure. Instead, we find that the negative Seebeck coefficient is due to *subtle defect-induced changes* of the electronic structure that occur already for small concentrations of Co_Z and, to a lesser extent, of Vc_{Co} defects. Both defect types are likely to occur in Co-rich and Co-poor samples: While E_{form} of Vc_{Co} may even be negative, Co_Z has a formation energy of only 0.30 eV in Co_2TiSi and 0.45 eV in Co_2TiGe, being second lowest after Vc_{Co}. Hence, both for surplus or a deficiency of Co, the defects with the lowest formation energy induce a negative thermovoltage. Thus, the results of our calculations help to rationalize the experimental findings at low temperatures. In addition, we point out that, both in ideal Ti-derived Heusler alloys as well as in many defected materials (Co_{Ti}, Ti_Z, Z_{Ti}), the minority-spin electrons start to contribute to the conductivity, and hence also to the Seebeck coefficient. This is another factor responsible for a persistently negative Seebeck coefficient at higher temperatures.

With the Curie temperature of the $\text{Co}_2\text{Ti}Z$ lying in the range of 380–400 K [20], spin fluctuations are expected to start to play a role at room temperature and above. Via the pertinent scattering mechanisms for the charge carriers, they might also have an impact on the Seebeck coefficient in this temperature range. Investigations of such complex effects, also including the temperature-induced lattice vibrations as well as a detailed analysis on the spin dependence of the Seebeck coefficient, will be the subject of future work.

In summary, the presented computational results highlight the decisive role played by off-stoichiometry in Heusler compounds, which must be taken into account when one wishes to select materials from this class for specific applications. The thermopower is found to be a sensitive probe of the existence of defects, but remains difficult to interpret even with computational results at hand, in particular in cases where several contributing factors—different types of point defects, phonon, and magnon scattering—are superimposed.

ACKNOWLEDGMENTS

This work was supported by the German Research Foundation [Deutsche Forschungsgemeinschaft (DFG)] within the Priority Program 1538 “Spin Caloric Transport (SpinCaT)”, Project No. Po1895/1-2. The authors acknowledge the computing time granted by the John von Neumann Institute for Computing (NIC) and provided on the supercomputer JURECA at Jülich Supercomputing Center (JSC). Additional access to the Cray-XT6m supercomputer facility has been offered by the Center for Computational Sciences and Simulation (CCSS) at the University Duisburg-Essen.

[1] Y. G. Yu, X. Zhang, and A. Zunger, Phys. Rev. B **95**, 085201 (2017).

[2] J. Kübler, A. R. Williams, and C. B. Sommers, Phys. Rev. B **28**, 1745 (1983).

[3] H. C. Kandpal, G. H. Fecher, and C. Felser, J. Phys. D **40**, 1507 (2007).

[4] T. Graf, C. Felser, and S. S. Parkin, Prog. Solid State Chem. **39**, 1 (2011).

[5] I. Galanakis, P. H. Dederichs, and N. Papanikolaou, Phys. Rev. B **66**, 174429 (2002).

[6] I. Galanakis, K. Özdoğan, B. Aktaş, and E. Şaşioğlu, Appl. Phys. Lett. **89**, 042502 (2006).

[7] F. J. Yang, Y. Sakuraba, S. Kokado, Y. Kota, A. Sakuma, and K. Takanashi, Phys. Rev. B **86**, 020409 (2012).

[8] M. Jourdan, J. Minár, J. Braun, A. Kronenberg, S. Chadov, B. Balke, A. Gloskovskii, M. Kolbe, H. J. Elmers, G. Schönhense *et al.*, Nat. Commun. **5**, 3974 (2014).

[9] B. Hülsen, M. Scheffler, and P. Kratzer, Phys. Rev. Lett. **103**, 046802 (2009).

[10] G. Li, T. Taira, K. Matsuda, M. Arita, T. Uemura, and M. Yamamoto, Appl. Phys. Lett. **98**, 262505 (2011).

[11] T. Ishikawa, N. Itabashi, T. Taira, K.-I. Matsuda, T. Uemura, and M. Yamamoto, J. Appl. Phys. **105**, 07B110 (2009).

[12] H. Liu, Y. Honda, T. Taira, K. Matsuda, M. Arita, T. Uemura, and M. Yamamoto, Appl. Phys. Lett. **101**, 132418 (2012).

[13] C. Sterwerf, M. Meinert, J. M. Schmalhorst, and G. Reiss, IEEE Trans. Magn. **49**, 4386 (2013).

[14] S. Chadov, T. Graf, K. Chadova, X. Dai, F. Casper, G. H. Fecher, and C. Felser, Phys. Rev. Lett. **107**, 047202 (2011).

[15] D. Comtesse, B. Geisler, P. Entel, P. Kratzer, and L. Szunyogh, Phys. Rev. B **89**, 094410 (2014).

[16] B. Geisler, P. Kratzer, and V. Popescu, Phys. Rev. B **89**, 184422 (2014).

[17] B. Geisler and P. Kratzer, Phys. Rev. B **92**, 144418 (2015).

[18] M. Meinert, J. Schmalhorst, H. Wulfmeier, G. Reiss, E. Arenholz, T. Graf, and C. Felser, Phys. Rev. B **83**, 064412 (2011).

[19] M. T. Dau and J. Herfort, J. Phys. D: Appl. Phys. **48**, 025003 (2015).

[20] J. Barth, G. H. Fecher, B. Balke, S. Ouardi, T. Graf, C. Felser, A. Shkabko, A. Weidenkaff, P. Klaer, H. J. Elmers *et al.*, Phys. Rev. B **81**, 064404 (2010).

[21] S. C. Lee, T. D. Lee, P. Blaha, and K. Schwarz, J. Appl. Phys. **97**, 10C307 (2005).

[22] V. Sharma, A. K. Solanki, and A. Kashyap, J. Magn. Magn. Mater. **322**, 2922 (2010).

[23] B. Balke, S. Ouardi, T. Graf, J. Barth, C. G. Blum, G. H. Fecher, A. Shkabko, A. Weidenkaff, and C. Felser, Solid State Commun. **150**, 529 (2010).

[24] C. G. Van de Walle and J. Neugebauer, J. Appl. Phys. **95**, 3851 (2004).

[25] S. B. Zhang, S.-H. Wei, and A. Zunger, Phys. Rev. Lett. **78**, 4059 (1997).

[26] R. Stern, B. Dongre, and G. K. H. Madsen, Nanotechnology **27**, 334002 (2016).

[27] P. Soven, Phys. Rev. **156**, 809 (1967).

[28] D. W. Taylor, Phys. Rev. **156**, 1017 (1967).

[29] P. Soven, Phys. Rev. B **2**, 4715 (1970).

[30] H. Ebert, D. Ködderitzsch, and J. Minár, Rep. Prog. Phys. **74**, 096501 (2011).

[31] H. Ebert, J. Braun, D. Ködderitzsch, and S. Mankovsky, Phys. Rev. B **93**, 075145 (2016).

[32] The Munich SPR-KKR package, H. Ebert *et al.*, http://www.ebert.cup.uni-muenchen.de/SPRKKR.

[33] W. H. Butler, Phys. Rev. B **31**, 3260 (1985).

[34] J. Banhart, H. Ebert, and J. Voitländer, Solid State Commun. B **139**, K19 (1987).

[35] Y. Kota, H. Tsuchiura, and A. Sakuma, J. Phys.: Conf. Ser. **200**, 052012 (2010).

[36] J. Kudrnovský, V. Drchal, and I. Turek, Phys. Rev. B **88**, 014422 (2013).

[37] J. P. Perdew, K. Burke, and M. Ernzerhof, Phys. Rev. Lett. **77**, 3865 (1996).

[38] P. Giannozzi, S. Baroni, N. Bonini, M. Calandra, R. Car, C. Cavazzoni, D. Ceresoli, G. L. Chiarotti, M. Cococcioni, I. Dabo *et al.*, J. Phys.: Condens. Matter **21**, 395502 (2009).

[39] D. Vanderbilt, Phys. Rev. B **41**, 7892 (1990).

[40] M. Methfessel and A. T. Paxton, Phys. Rev. B **40**, 3616 (1989).

[41] H. J. Monkhorst and J. D. Pack, Phys. Rev. B **13**, 5188 (1976).

[42] S. Picozzi, A. Continenza, and A. J. Freeman, Phys. Rev. B **66**, 094421 (2002).

[43] H. C. Kandpal, V. Ksenofontov, M. Wojcik, R. Seshadri, and C. Felser, J. Phys. D **40**, 1587 (2007).

[44] A side-by-side comparison of ASA vs FP density of states curves in Co_2TiSn is shown in Fig. 5 of Ref. [43]. While the FP approaches predict this compound as being half metallic, it is metallic in the ASA-based calculations.

[45] P. J. Webster and K. R. A. Ziebeck, J. Phys. Chem. Solids **34**, 1647 (1973).

[46] A. W. Carbonari, R. N. Saxena, W. Pendl, Jr., J. Mestnik Filho, R. N. Attili, M. Olzon-Dionysio, and S. D. de Souza, J. Magn. Magn. Mater. **163**, 313 (1996).

[47] S. Wimmer, D. Ködderitzsch, and H. Ebert, Phys. Rev. B **89**, 161101 (2014).

[48] Here the off-diagonal elements of the tensors $\underline{L}^{(0)}$ and $\underline{L}^{(1)}$ connected to the anomalous Hall and Nernst effects were neglected. In cubic metals this assumption is in general well justified by the significantly smaller magnitude of these purely antisymmetric tensor elements in comparison to the diagonal ones.

[49] Materials Project, https://materialsproject.org, and references therein. See also the AFLOW project at http://materials.duke.edu/apool.html and references therein.

[50] R. V. Chepulskii and S. Curtarolo, Acta Mater. **57**, 5314 (2009).

[51] In Ref. [50], the Co_2Ti most stable crystal structure is predicted to be $C14$, with a formation energy lying 0.022 eV/f.u. below that of $C15$.

[52] C. Colinet, J.-C. Tedenac, and S. G. Fries, Calphad **33**, 250 (2009).

[53] B. Hülsen, M. Scheffler, and P. Kratzer, Phys. Rev. B **79**, 094407 (2009).

[54] M. Kogachia, S. Kikuchia, T. Fujiwaraa, and F. Horib, J. Alloys Compd. **480**, 462 (2009).

[55] M. Nagasako, Y. Taguchi, T. Miyamoto, T. Kanomata, K. R. A. Ziebeck, and R. Kainuma, Intermetallics **61**, 38 (2015).

[56] T. Nobata, G. Nakamoto, M. Kurisu, Y. Makihara, K. Ohoyama, and M. Ohashi, J. Alloys Compd. **347**, 86 (2002).

[57] S. Picozzi, A. Continenza, and A. J. Freeman, Phys. Rev. B **69**, 094423 (2004).

[58] J. S. Faulkner and G. M. Stocks, Phys. Rev. B **21**, 3222 (1980).

[59] P. Mavropoulos, K. Sato, R. Zeller, P. H. Dederichs, V. Popescu, and H. Ebert, Phys. Rev. B **69**, 054424 (2004).

[60] K. Özdoğan, E. Şaşioğlu, and I. Galanakis, Phys. Status Solidi (RRL) **1**, 184 (2007).

[61] B. A. Alhaj and B. Hamad, J. Phys. Chem. Solids **74**, 265 (2013).

[62] N. T. Mahmoud, J. M. Khalifeh, B. A. Hamad, and A. A. Mousa, Intermetallics **33**, 33 (2013).

[63] S. J. Watzman, R. A. Duine, Y. Tserkovnyak, S. R. Boona, H. Jin, A. Prakash, Y. Zheng, and J. P. Heremans, Phys. Rev. B **94**, 144407 (2016).